Bull. Mater. Sci. (2020) 43:8
https://doi.org/10.1007/s12034-019-1973-3
© Indian Academy of Sciences

Study on the corrosion and wear characteristics of magnesium alloy AZ91D in simulated body fluids

R VAIRA VIGNESH, R PADMANABAN* and M GOVINDARAJU
Department of Mechanical Engineering, Amrita School of Engineering, Amrita Vishwa Vidyapeetham, Coimbatore 641112, India
*Author for correspondence (dr_padmanaban@cb.amrita.edu)

MS received 7 June 2017; accepted 24 June 2019; published online 17 December 2019

Abstract. Bioimplants made of metallic materials induce a stress-shielding effect and delayed osteoblast activity during *in-vivo* experiments. Bioimplants also suffer corrosion, wear and combined effect of corrosion–wear during their service time. Bioimplants made of magnesium alloys result in a negligible stress shielding effect, owing to their similarity with bone's elastic modulus. However, the soft matrix of the magnesium alloy is susceptible to high-wear rates. In this study, magnesium alloy AZ91D is subjected to the corrosion test (immersion and electrochemical), adhesive wear and simultaneous corrosion–wear test to test the significance of the body fluid in the corrosion–wear rate of the bioimplants. The surface morphology, elemental composition and phase composition of the specimens are characterized using field emission scanning electron microscopy, energy dispersive X-ray spectroscopy and X-ray diffraction analytic techniques. The results indicate that the simulated-body fluid has a significant effect on the corrosion rate and corrosion–wear rate of the specimens.

Keywords. Magnesium alloy; adhesive wear; corrosion; simulated-body fluid; radial-basis function.

1. Introduction

The biocompatible nature has enabled magnesium and magnesium alloys as one of the candidature materials for bioimplant applications [1,2]. The first response of the human immune system to bioimplant is the adhesion of protein to the surface of the bioimplants. This protein coating corrodes the bioimplant material. Due to high chemical activity, bioimplants made of magnesium alloys are prone to high corrosion rates with evolution of hydrogen gas [3,4]. The rapid evolution of hydrogen gas during corrosion of the bioimplant is a lethal phenomenon to the neighbouring tissues [5]. Therefore, the bioimplants should be engineered to withstand the effects of protein coating, physiological pH, chloride ions from physiological fluid, a change in human body temperature and have a controlled corrosion rate.

The first generation of biomedical bioimplants stressed on the physical properties similar to that of the replaced bone and minimized toxicity to the neighbouring tissue [6,7]. The second generation of biomedical bioimplants emphasized on the ability of the biomaterials to (i) interact with a physiological environment, (ii) enhance tissue bonding and osteoblast activity and (iii) degrade progressively with healing of tissues or bone. The current third generation of bioimplants is designed to stimulate the precise cellular response at the molecular level [8–13]. The material chosen for biodegradable bioimplant should have a gradual loss in mechanical strength and materials by corrosion, which should be counteracted by the newly forming bone [14,15]. With mechanical properties similar to that of bone, magnesium alloy AZ91D could be used for bioimplants. However, the corrosion rate of AZ91D is rapid in the chloride containing physiological environment. The corrosion rate and hence the properties of AZ91D could be contrived using various processing or coating techniques such as heat treatment, micro-arc oxidation, vapour deposition.

Nishio *et al* [16] found that the microstructure of the unidirectionally solidified AZ91D alloy consisted of α phase and nanosized β-phase particle dispersion. The dispersion of the β phase increased tensile strength (TS) of the processed alloy by two folds. Mabuchi *et al* [17] found that the isotropic grain shape of the directionally solidified AZ91D alloy enhanced the TS and proof stress at 200°C. Shanthi *et al* [18] compared the wear behaviour of the recycled AZ91D alloy (mechanical milling) and cast AZ91D alloy. The fine-grained structure produced by a mechanical milling process did not increase the adhesive wear resistance, over a range of velocity at a normal load of 10 N. Zafari *et al* [19] found the critical temperature for transition of wear from mild to severe in the AZ91D alloy at various normal loads. Severe plastic deformation was observed at a normal load of 40 N and at a testing temperature of 100°C. The formation of oxide

Electronic supplementary material: The online version of this article (https://doi.org/10.1007/s12034-019-1973-3) contains supplementary material, which is available to authorized users.

layers at a lower normal load of 5 N increased the wear resistance at temperatures of 100–250°C. Severe softening of the alloy at temperatures above 300°C, dramatically reduced the wear resistance of the alloy.

Zafari *et al* [20] found that the formation of the oxide layer decreased the wear rate of AZ91D by 8% while the wear rate increased with an increase in test temperature beyond 100°C. Softening of the β phase and formation of more slip systems, reduced the hardness and wear resistance. Chen and Alpas [21] found that an increase of contact temperature above 74°C, induced severe wear in the AZ91D alloy during the adhesive wear test. The wear rate and contact temperature increased with a sliding distance during dry sliding wear tests.

Witte *et al* [22] found that AZ91D has good biocompatibility and corrosion resistance in *in-vivo* studies. Choudhary *et al* [23] found that the AZ91D alloy is susceptible to stress corrosion cracking in simulated body fluid (SBF) solution in the regime of a low strain rate. They observed transgranular cracks in the fractured specimens, though intergranular SCC and combined SCC were prevalent in the AZ91D alloy. Xue *et al* [24] found that the *in-vivo* corrosion rate of the AZ91D alloy was lower than the *in-vitro* corrosion rate (SBF at 37°C). No biocompatibility issues were observed for an implantation period of two months. Walter *et al* [25] investigated the effect of surface roughness on the polarization resistance of the AZ91D alloy tested in SBF and found that the alloy with the rough surface had lower polarization resistance than the smooth-surfaced alloy. The severity of localized degradation was higher for the specimen with a rough surface. Tahmasebifar *et al* [26] studied the effect of pressure-moulding process variables on the cell adhesion and the proliferation properties of the AZ91D alloy. The plates with high porosity and rough texture increased the cell adhesion and proliferation. Wen *et al* [27] studied the bio-degradability and surface chemistry of AZ31D and AZ91D alloys subjected to immersion and electrochemical tests in modified SBF. With an increase in the immersion period from 1 day to 24 days, the corrosion rate of AZ91D was significantly lower than that of AZ31D.

The mechanical and tribological behaviour of alloys depend on the corrosivity of the environment, in which the alloys deliver their functionality. Therefore, a study to investigate the effect of a corrosive physiological environment on the wear rate of the AZ91D alloy becomes obligatory. In this study, an attempt has been made to analyse the effect of the corrosive SBF environment (Dulbecco's phosphate-buffered solution) on the wear rate of the AZ91D specimens. The effect of wear process parameters on the adhesive wear rate and corrosion–wear rate was also investigated. A hybrid model (polynomial function and radial basis function (RBF)) was developed to investigate the effect of adhesive wear parameters of the process on the wear rate of specimens. The corrosion rate of AZ91D was evaluated by conducting an immersion test and electrochemical corrosion test. The influence of corrosion products on the corrosion mechanism of AZ91D in SBF was also investigated.

2. Materials and methods

2.1 *Base material*

A rolled AZ91D plate with a thickness of 4 mm was used in the study. Chemical composition was analysed using optical emission spectroscopy and the composition is given in table 1.

2.2 *Base material characterization*

2.2a *Microstructure*: Specimens of dimension 10 mm× 10 mm were cut from the base material and mounted using a cold-setting compound. The surface of the specimens was prepared as outlined by the standard ASTM E3-11. The surface of the specimen was prepared using an automatic disc grinder using different grades of the abrasive sheet, starting from a coarse grade abrasive sheet to a very-fine grade abrasive sheet. A mirror polish was obtained in the specimen by polishing the specimen in diamond slurry, which was followed by polishing in the alumina suspension against soft velvet cloth. This was followed by the etchant which was prepared by mixing 100 ml of 95% ethanol, 6 g picric acid, 5 ml acetic acid and 10 ml distilled water, as prescribed by ASTM E407-07. The polished surface of the specimens was etched for 10 s by a gentle swab using cotton dipped in the etchant, which was in turn followed by a cold water rinse. The microstructure was observed in an optical microscope (Make: Carl Zeiss, Model: Axiovert 25).

2.2b *Microhardness test*: As described in section 2.2a, the specimens were prepared for the microhardness test (unetched). Vicker's microhardness measurements were made using a microhardness tester (Make: Mitutoyo, Model: MVKH1) as outlined by the standard IS 1501:2002. The diamond indentor was plunged into the specimen under an axial load of 9.80 N and the indentor was withdrawn after 15 s.

2.2c *Tensile test*: The specimens for the tensile test were prepared and tested in a universal testing machine (Make: Tinius Olsen, Model: H25KT) as per the guidelines of the standard ASTM B557-10. The dimensions of the tensile test specimens are as follows: gauge length: 50.8 mm, reduced section width: 12.7 mm, reduced section length: 57.2 mm, width of grip section: 19.0 mm and length of grip section: 50.8 mm. The stress–strain graph was plotted by increasing the strain (incremental value of 0.01) and obtaining the force correspondingly. The yield strength was determined by the offset method (0.2%).

2.3 *Corrosion and wear tests*

2.3a *Immersion corrosion test*: The immersion test was performed to assess the change in pH of the SBF and the corrosion rate of the base material with an increase in time. The SBF used for the immersion test was Dulbecco's phosphate-buffered solution. The specimens for the immersion test were

Table 1. Composition of the as-cast AZ91D alloy.

Element	Al	Zn	Si	Mn	Fe	Cu	Ni	Mg
Composition, wt%	8.72	0.51	0.04	0.31	0.001	0.002	0.01	Balance

Table 2. Composition of Dulbecco's phosphate-buffered solution.

Sl. no.	Component name	Chemical formula	Concentration, mg l^{-1}
1	Anhydrous calcium chloride	$CaCl_2$	100
2	Anhydrous magnesium chloride	$MgCl_2$	47
3	Potassium chloride	KCl	200
4	Potassium phosphate monobasic	KH_2PO_4	200
5	Sodium chloride	NaCl	8000
6	Anhydrous sodium phosphate dibasic	Na_2HPO_4	1150

prepared and tested in SBF as per the guidelines of the standard ISO 10993-15. The composition of the SBF solution is given in table 2. The temperature of the solution was maintained at 37 ± 0.1°C using a temperature-controlled water bath and the pH of the SBF solution was measured using a pH metre with a sensitivity of ±0.01.

2.3b *Electrochemical corrosion test*: The specimens for the electrochemical corrosion test were cut from the base material to the required dimension of 60 mm × 10 mm × 4 mm. The surface of the specimens was prepared as per the procedure outlined in section 2.2a and degreased with acetone. The prepared specimens were placed in a desiccator filled with calcium chloride ($CaCl_2$) to avoid the ill effects of moisture and air. The specimens were masked using an insulation tape and an area of 1 mm^2 was left unmasked for exposure to SBF solution, which is Dulbecco's phosphate-buffered solution. The electrolyte solution was prepared by mixing the essential amount of salts in distilled water as listed in table 2. The specimen (working electrode), platinum wire (counter electrode) and standard calomel electrode (reference electrode) constituted the electrochemical cell setup. The electrochemical cell setup was immersed in a water bath, which was maintained at a physiological temperature of 37±0.1°C and a physiological pH of 7.

Potentiodynamic polarization is one of the techniques in an electrochemical corrosion test used to deduce the corrosion current density, from the net current of anodic and cathodic polarization by polarizing the test specimen in the electrolyte. Electrochemical workstation (Make: CH Instruments, Model: 680 Amp Booster) was used to perform the potentiodynamic polarization test. The potentiodynamic polarization test was performed in line with the standard ASTM G5-94. Open-circuit potential was established for the specimen for an immersion period of 120 min and that potential was chosen as the reference potential for conducting the potentiodynamic polarization tests. The specimens were polarized at a scan rate of 5 mV s^{-1} in the potential range of −2.5 to +2 V. The current sensitivity was chosen as 10^{-1} μA for the ECC tests.

2.4 *Adhesive wear test*

AZ91D samples of dimension 10 mm × 10 mm were mounted in a steel hollow tube with an outer diameter of 12 mm, inner diameter of 10 mm and height of 50 mm, using a cold-setting compound to prepare adhesive-wear test specimens. The specimens were cleaned with acetone and weighed using a precision weighing balance with a readability of 0.0001 g. The wear test was conducted at par with the guidelines of the standard ASTM G99-95a in a pin on disc wear tester (Make: Ducom, Model: TR20LE). The wear test parameters chosen for the study were loaded at the wearing contact (load), relative sliding speed between the contacting surfaces (velocity) and accumulated sliding distance (distance).

2.4a *Statistical modelling*: A face-centred central composite design was used to develop the design matrix and generate a mathematical model to interrelate the wear-test parameters with the wear rate of the specimens. The chosen level of process parameters and the design matrix for experimental trials for the adhesive wear test is given in table 3.

The regression models developed by response-surface designs could not map the response variables that have complex non-linearity characteristics with the input process parameters [28]. A hybrid model integrating the polynomial function and RBF was developed to study the effect of wear process parameters on the adhesive wear rate of the specimens. The RBF is a special class of function and it is typically of Gaussian type [29]. The advantage of multiquadratic RBF over Gaussian type is that it delivers a finite-global response and it is given by equation (1) [30].

$$f(x) = \frac{\sqrt{r^2 + (x - c)^2}}{r} \tag{1}$$

Table 3. Design matrix and experimental results of the adhesive wear test.

	Coded			Real			
Sl. no.	Load	Velocity	Distance	Load, N	Velocity, m s^{-1}	Distance, m	Wear rate (10^{-6}), g N^{-1} m^{-1}
AW1	−1	−1	−1	9.8	1	600	0.3911
AW2	1	−1	−1	29.4	1	600	0.4535
AW3	−1	1	−1	9.8	3	600	3.4694
AW4	1	1	−1	29.4	3	600	1.9785
AW5	−1	−1	1	9.8	1	1200	2.8316
AW6	1	−1	1	29.4	1	1200	2.0493
AW7	−1	1	1	9.8	3	1200	12.3300
AW8	1	1	1	29.4	3	1200	6.7857
AW9	0	0	0	19.6	2	900	2.3413
AW10	0	0	0	19.6	2	900	2.5680
AW11	0	0	0	19.6	2	900	2.3243
AW12	0	0	0	19.6	2	900	2.4603
AW13	−1	0	0	9.8	2	900	3.4240
AW14	1	0	0	29.4	2	900	1.1451
AW15	0	−1	0	19.6	1	900	2.7381
AW16	0	1	0	19.6	3	1000	1.6480
AW17	0	0	−1	19.6	2	600	2.3129
AW18	0	0	1	19.6	2	1200	2.2747
AW19	0	0	0	19.6	2	900	2.4943
AW20	0	0	0	19.6	2	900	2.3929

Multiquadratic RBF was chosen to build the model for the response variable (adhesive wear rate). The characteristic equation for function approximation using the RBF network is given by equation (2).

$$\mathrm{RBF} = f(x) = \sum_{i=1}^{n} w_i * \emptyset(||x - x_i||) \tag{2}$$

where $f(x)$ is the approximation function, n is the number of RBFs and w_i's are the weights. The characteristic polynomial function—RBF mathematical model is given by equation (3).

$$y(x) = \mathrm{PF} + \mathrm{RBF} \tag{3}$$

where y is the response variable, PF is the polynomial function and RBF is the radial basis function. If the polynomial function is of degree 1, a linear-RBF is obtained.

2.5 *Corrosion–wear test*

A new approach was established to study the combined effect of corrosion and wear rates of the specimens. The SBF was heated to 37 ± 0.1°C using a temperature-controlled water bath. The flow of the SBF was controlled using a control valve. The specimens were clamped in the adhesive-wear tester and the setup was confined using an enclosure. The wear test was performed in accordance with the standard ASTM G99-95a with the flow of SBF (corrosive liquid). The corrosion–wear test parameters were chosen similar to that of adhesive-wear test parameters to explicitly study the effect of SBF fluid on the corrosive–wear rate of the specimens.

2.6 *Metallurgical characterizations of post corrosion and wear tests*

The surface morphologies of the specimens subjected to the tensile test, immersion test, electrochemical corrosion test, adhesive wear test and corrosion wear test were observed using a field-emission scanning electron microscope (FE-SEM) (Make: Zeiss Sigma). The images were obtained at electron acceleration voltages of 5 and 10 kV at various levels of magnification. The elemental composition and the elemental map of the corroded specimens were determined using energy-dispersive X-ray spectroscopy (EDS) (Bruker). The constitutional phases of the base material, adhesive wear test debris and corrosion–wear test debris were analysed using an X-ray diffractometer (Rigaku, Model: Ultima 4). The X-ray diffraction (XRD) results of the specimens were obtained at continuous-scanning mode using copper Kα radiation at a scan rate of 2° min^{-1}.

3. Results and discussion

3.1 *Base material characterization*

3.1a *Microstructure*: The optical micrograph of the base material at 200× magnification displaying well-developed α-Mg (α phase) dendrites with secondary arms is shown in

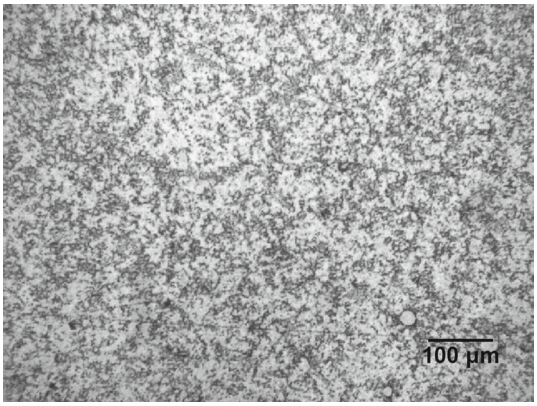

Figure 1. Microstructure of AZ91D alloy depicting the α phase (dark region), β phase (bright region) and (α + β) eutectic phase (grey region).

figure 1. Beyond the solubility limit of Al in Mg, a brittle intermetallic secondary phase β-$Mg_{17}Al_{12}$ (β phase) precipitated out from the supersaturated primary phase (α phase) of the alloy. The phases present in the base material are identified as the α phase, β phase and (α + β) eutectic phase. Picric acid in the etchant darkened the α phase and therefore the α phase/β phase was observed as the dark region/bright region in the micrograph, respectively. The coarse branched structure observed at the grain boundaries and in the interdendritic region (grey region) was identified as the eutectic phase. XRD analysis was performed to investigate the existing phases present in the base material AZ91D. As shown in supplementary figure S1, distinct diffraction peaks were observed for the α phase and β phase of the alloy AZ91D. Owing to the lesser concentration of Zn in the matrix, diffraction peaks of Mg–Zn phases were not detected.

3.1b *Microhardness*: Vicker's microhardness was measured along a horizontal line in the specimen at 10 instances that were located at a distance of 1 mm from the previous instance (indentation). The average microhardness of the base material was found to be 57.9 ± 3.15 Hv. The standard error of the measurements was 0.996438.

3.1c *Tensile test*: The stress–strain graphs of three tensile test specimens are shown in supplementary figure S2. The test specimens exhibited an average yield strength (offset = 0.2%) of 135 MPa. As shown in figure 2, large porosities and oxide layers were observed in the FE-SEM fractography of the fractured surface. The fractured surface with dimples as primary feature indicated ductile fracture [31,32]. The β-phase network at the grain boundaries tends to crack or debond from the matrix under lower stress during tensile deformation [33]. Therefore, brittle fracture was observed at some instances on the fractured surface.

3.2 *Corrosion and wear test*

3.2a *Immersion test*: The concentration of the hydrogen ions (H^+) in the SBF was measured using a pH metre. It is observed from supplementary figure S3(a) that the concentration of H^+ in SBF decreases with an increase in the immersion period. This indicated the evolution of H_2 gas as a result of the corrosion phenomenon on the surface of the specimens. The corrosion products on the surface of the specimens immersed in SBF were cleaned using chromic acid and then the mass loss was calculated. The rate of variation of mass decreased and became stable with an increase in the immersion time. The corrosion rate of the specimens immersed in SBF for different intervals of time is shown in supplementary figure S3(b). The corrosion rate of the specimen after 24 h of immersion was 4.37 mm $year^{-1}$. The corrosion rate steadily decreased and stabilized at an average corrosion rate of 1.05 mm $year^{-1}$ after 144 h of immersion. The corrosion rate of the specimens decreased by a factor of 50, 29, 22, 10, 0.23 and 0.02% in the proceeding days of immersion.

The surface morphology of the specimens was observed using FE-SEM after immersion in SBF for different time

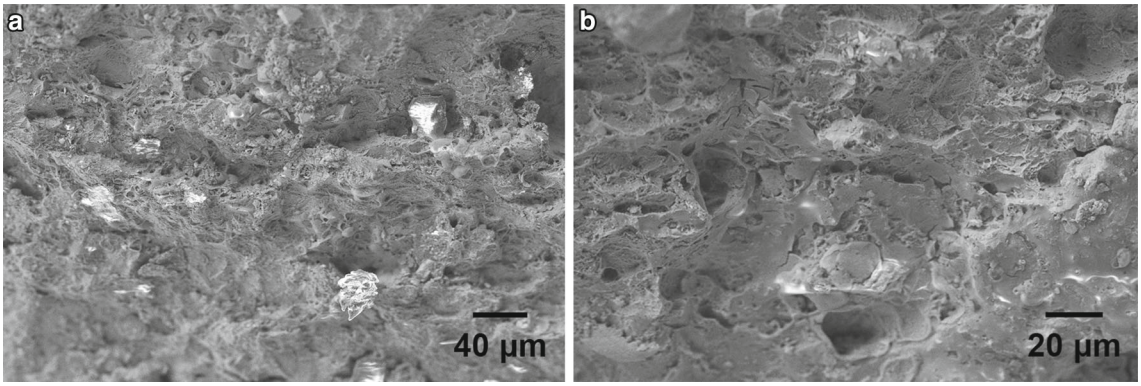

Figure 2. Fractography of the tensile test specimen at magnification of 4000× showing dimples and ruptured surface indicating a combined ductile and brittle fracture mechanism.

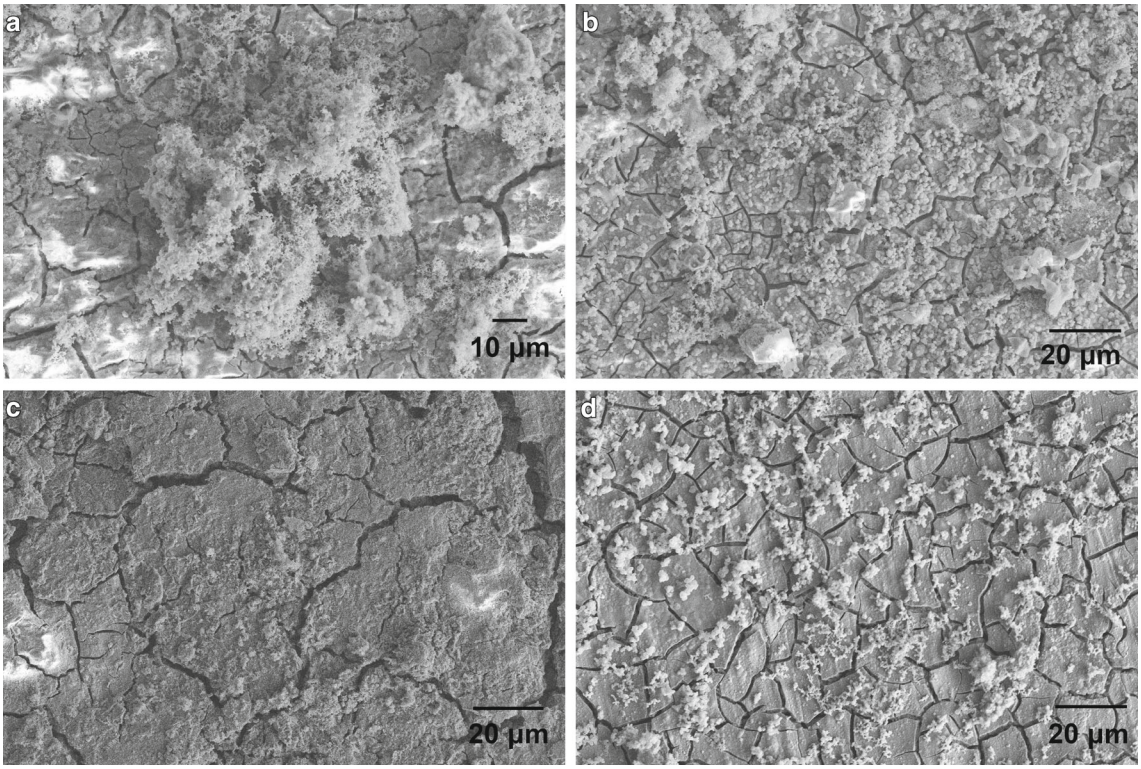

Figure 3. Surface morphology of the specimen (**a**) IC1 after 24 h of immersion showing flower-like clusters; (**b**) IC3 after 72 h of immersion with diminished flower-like clusters; (**c**) IC5 after 120 h of immersion showing wide cracks and a few flower-like clusters and (**d**) IC7 after 168 h of immersion showing a few flower-like clusters and a thin layer of corrosion products on the surface.

lengths. The surface of the specimens IC1, IC3, IC5 and IC7 is shown in figure 3(a)–(d), respectively. The surface was covered by a corrosion layer, with many shallow cracks and micropores on its surface. During initial hours of immersion, the formation of the $Mg(OH)_2$ layer acted as a barrier to prevent the matrix from absorbing Ca and P from the SBF. The $Mg(OH)_2$ layer is vulnerable in the presence of chloride ions (Cl^-) [34]. The presence of Cl^- ions in SBF and the layered structure of $Mg(OH)_2$ cracked the continuous corrosion layer of $Mg(OH)_2$ [15]. Flower-like clusters bloomed over the surface of the specimen after an immersion period of 24 h, as shown in figure 3(a). As observed from figure 3(d), the flower-like structures fell off from the surface, with an increase in the immersion time. The deposition of the corrosion products suppressed the corrosion rate of the specimens and reached a stable state after 144 h of immersion. The flower-like corrosion products could be magnesium carbonate, sulphate or phosphate.

EDS analysis was performed on the corroded specimen to quantify the elements present in the corrosion products. The results of the EDS analysis of the corroded specimens after 24 h (IC1) and 168 h (IC7) of immersion are given in table 4. The peaks indicated the presence of Mg, Na, Ca, P, Cl and O elements in the corrosion products. During the initial period of immersion, an increase in the Ca/P ratio increased the corrosion rate of the specimens. However, the Ca/P ratio decreased with an increase in the immersion time, reducing the corrosion rate. The reduction in Ca on the surface of the corroded specimen favoured the formation of a hydroxyapatite layer ($Ca_{10}(PO_4)_6(OH)_2$) or calcium magnesium phosphate layer ($Ca_{10-x}Mg_x(PO_4)_6(OH)_2$) [8–10,13]. Previous studies proved that the formation of the hydroxyapatite layer on the bioimplant material supports the bone growth and bioimplant—bone integration [22,35]. Elemental mapping of Mg, Al, Ca, P and O in the corroded area of specimens IC1 and IC7 is shown in figure 4(a) and (b), respectively. The elemental mapping revealed that the corrosion products increased with an increase in the immersion time. The high concentration of Ca and P in the corrosion layer of the specimen IC7 is attributed to the Ca–P salt containing Mg and/or $Mg(OH)_2$.

XRD analysis of the corroded specimen IC7 is shown in the supplementary figure S4. Prominent peaks were detected for the α phase and β phase. Less intense peaks of MgO and $Mg(OH)_2$ were also detected in XRD. Besides many peaks present in the 2θ range between 20 and 35° confirmed the presence of $Ca_{10}(PO_4)_6(OH)_2$ or $Ca_{10-x}Mg_x(PO_4)_6(OH)_2$ on the corrosion layer.

The corrosion mechanism of the AZ91D alloy is significantly influenced by microstructural phases in the alloy

Table 4. EDS analysis of the specimens corroded in the immersion test.

		Normalized concentration, wt%		Atomic concentration, wt%		Error (3σ), wt%	
Sl. no.	Element	IC1	IC7	IC1	IC7	IC1	IC7
1	Aluminium	0.16	0.11	0.13	0.09	0.10	0.10
2	Magnesium	12.32	15.97	11.17	14.59	1.42	1.88
3	Sodium	1.40	1.93	1.34	1.86	0.28	0.36
4	Potassium	0.07	0.05	0.04	0.03	0.09	0.09
5	Calcium	21.98	18.74	12.08	10.38	0.12	1.22
6	Chlorine	0.46	0.60	0.29	0.38	1.35	0.13
7	Oxygen	44.61	41.41	61.43	57.48	11.55	11.22
8	Phosphorous	19.01	21.19	13.52	15.19	1.53	1.77
	Total	100	100	100	100	—	—

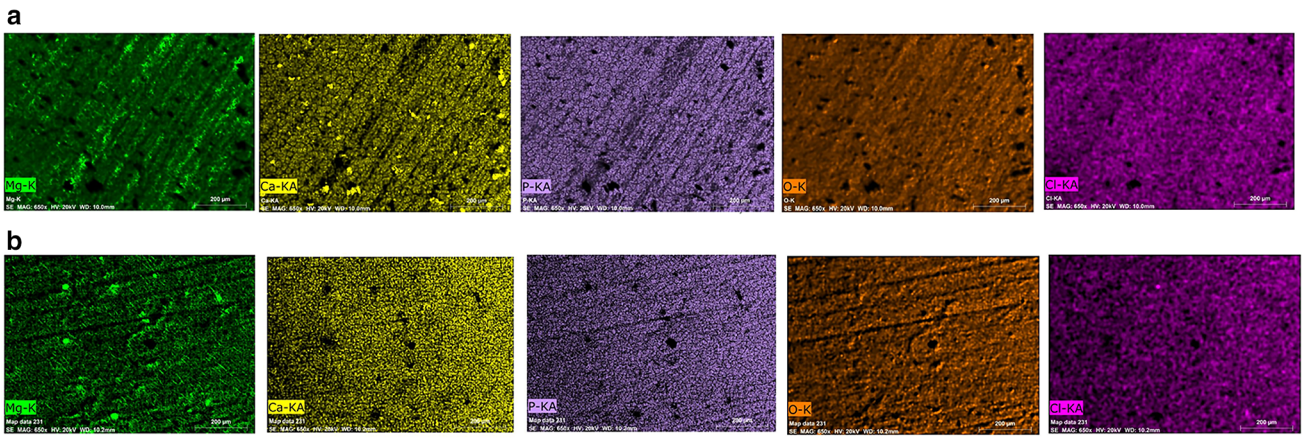

Figure 4. Elemental mapping of the specimen (**a**) IC1 after 24 h of immersion and (**b**) IC1 after 168 h of immersion indicating the high deposition of Ca and P on the surface.

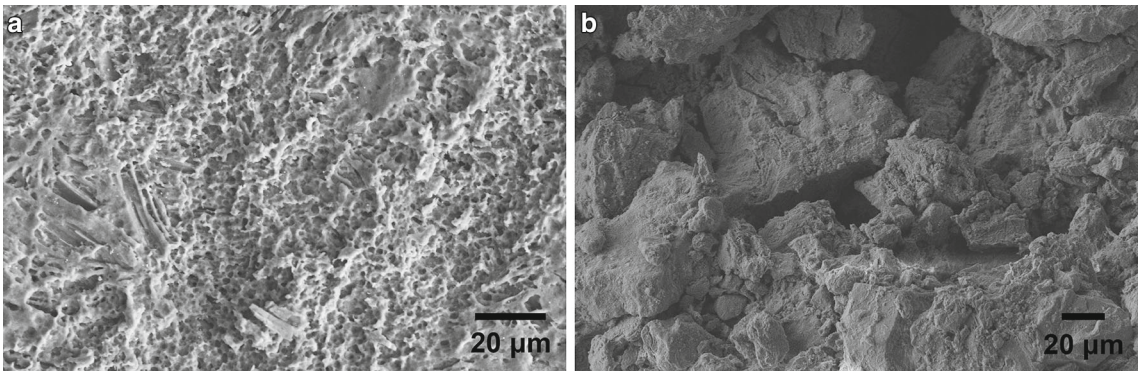

Figure 5. (**a**) Surface of the specimen IC7 after cleaning the corrosion products showing protrusion (β phase) and shallow pits (α phase, which was dissolved by chromic acid) and (**b**) surface morphology of AZ91D after the potentiodynamic polarization test showing micropores at magnification of 3000×.

matrix and the composition of the SBF solution. As shown in figure 5(a), many circle-like patches were observed on the FE-SEM image of the specimen IC7 after the removal of corrosion products using chromic acid. At higher magnification, protruded structures with shallow pits were observed. When the specimen IC7 was immersed in chromic acid, low-dissolution of the β phase resulted in protrusions, while high-dissolution of the α phase resulted in shallow pits. It

was observed that the dissolution propensity of the α phase, left relatively stable grain boundaries of the β phase. This attests that the β phase was homogeneously distributed in the matrix and acts as a barrier to corrosion.

3.2b *Electrochemical corrosion test*: After establishing a stable-open circuit potential, the specimen was potentiodynamically polarized from −2.5 to +2 V at a scan rate of 5 mV s^{-1}. The Tafel plot of the tested specimen is shown in supplementary figure S5. The electrochemical parameters extracted from the Tafel plot are as follows: corrosion current, $i_{corr} = 1.943 \times 10^{-6}$ A and corrosion potential, $E_{corr} = -1.448$ V. E_{corr} determines the thermodynamic tendency towards corrosion, while i_{corr} indicates the velocity of uniform corrosion. The corrosion current was converted to the corrosion rate using equation (4).

$$\text{Corrosion rate}\left(\text{mm year}^{-1}\right) = \frac{k \times i_{corr} \times E'}{A \times \rho} \tag{4}$$

where k is a constant (3272), E' is the equivalent weight in g per equivalent (12.1525 g per equivalent), A is the exposure area (0.01 cm^2) in cm^2 and ρ is the density (1.74 g cm^{-3}) of the specimen in g cm^{-3}. The corrosion rate calculated from the Tafel region was 4.44 mm $year^{-1}$. The corrosion rate calculated from the mass loss of the specimen was found to be lower than the corrosion rate calculated from the Tafel region. The surface morphology of the corrosion specimen is shown in figure 5(b). The presence of micropores and cavities on the surface of the corroded specimen indicated the high-corrosion rate of the specimen in the potentiodynamic polarization test.

During the initial-immersion period of the specimen, Mg in the alloy matrix dissolves and forms a corrosion layer of $Mg(OH)_2$. The equations describing the reaction on the surface of the specimen are given by equations (4 to 6). The corrosion layer $Mg(OH)_2$ was stirred by the evolution of H_2 gas, which promotes further corrosion of the specimen.

$$Mg \rightarrow Mg^{2+} + 2e^- \tag{5}$$

$$2H_2O + 2e^- \rightarrow H_2\uparrow + 2OH^- \tag{6}$$

$$Mg^{2+} + 2OH^- \rightarrow Mg(OH)_2 \tag{7}$$

$Mg(OH)_2$ is relatively more active than Mg and hence they could be regarded as the defect sites that are ideally suited for corrosion in Cl^- ion rich environments. With an increase in the immersion time, the anodic reaction results in more dissolution of Mg^{2+} ions and more consumption of phosphate and carbonate ions from the SBF solution. This increased the Cl^- ion concentration in the SBF solution. Hence, the Cl^- ions are preferentially adsorbed on the specimen surface. Owing to its small radius, Cl^- ions penetrate the corrosion layer and converts $Mg(OH)_2$ to $MgCl_2$. The formation of $MgCl_2$ from $Mg(OH)_2$ is summarized in equation (8).

$$Mg(OH)_2 + 2Cl^- \rightarrow MgCl_2 + 2(OH)^- \tag{8}$$

The high solubility of $MgCl_2$ in the electrolyte creates many exposed sites on the surface, which enables more accessibility of Mg^{2+} ions to phosphate ions (HPO_4^{2-} or PO_4^{3-}), and Ca^{2+} ions in the SBF solution. This in turn resulted in the formation of $Ca_{10-x}Mg_x(PO_4)_6(OH)_2$ or $Ca_{10}(PO_4)_6(OH)_2$, in accordance with the published research [27,36]. The formation of such compact and insoluble phosphates retarded dissolution of Mg from the surface of the specimen. Hence, the corrosion rate of the specimens decreased with an increase in the immersion time, which is evident from the immersion test results given in section 3.2a. This layer reduced the permeability of Ca^{2+} and PO_4^{3-} ions into the interface between the corrosion layer and the matrix. Hence, the corrosion layer consisted of more Ca, P and O than other elements, which is in agreement with the result of the EDS element map. As evident from the literature, the difference in the corrosion potential between the α phase and β phase is ∼1 V. The α phase is more anodic with respect to the β phase, which induces microgalvanic corrosion in the matrix.

3.3 *Adhesive wear*

The adhesive wear test was performed by varying the wear test parameters namely normal load, sliding velocity and sliding distance at three levels as per face-centred central composite design. Equation (9) was used to calculate the wear rate of the specimens and the calculated wear rates are given in table 3.

$$\text{Wear rate}\left(\text{g N}^{-1}\,\text{m}^{-1}\right) = \frac{\Delta m}{F \times L} \tag{9}$$

The wear rate of the specimen AW1 tested at a load of 9.8 N, a sliding velocity of 1 m s^{-1} and a sliding distance of 600 m was found to be 0.3911×10^{-6} g N^{-1} m^{-1}, which was the least among the tested specimens. The metallographic examination of the worn out surface shows loose wear debris as seen in figure 6(a). The delamination of the surface oxide layer or subsurface material layer resulted in the formation of loose wear debris.

The wear rate was high (12.3300×10^{-6} g N^{-1} m^{-1}) for the specimen AW7 tested at a load of 9.8 N, a sliding velocity of 3 m s^{-1} and a sliding distance of 1200 m. The surface morphology of the worn out specimen AW7 displayed a severe-wear regime, which was characterized with massive surface deformation and large amounts of wear debris, as shown in figure 6(b). During the wear test, the material layer adjacent to the contact surface had suffered an extensive plastic deformation. These plastically deformed layers extruded out of the material surface, which was subsequently removed as flat wear debris particles. Hence, the worn out surface had deep grooves indicating severe wear of the specimens. XRD analysis of the wear

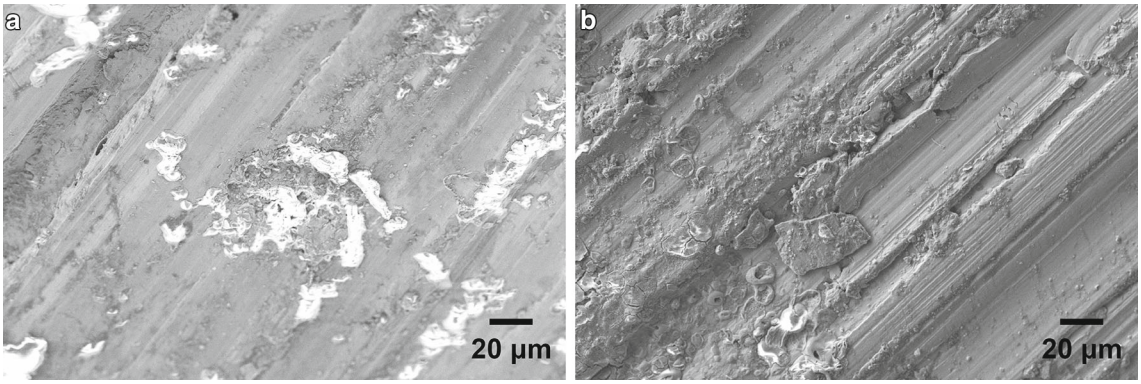

Figure 6. FE-SEM image of the specimen after the adhesive-wear test: (**a**) specimen AW1 exhibiting mild wear and (**b**) specimen AW7 exhibiting severe wear.

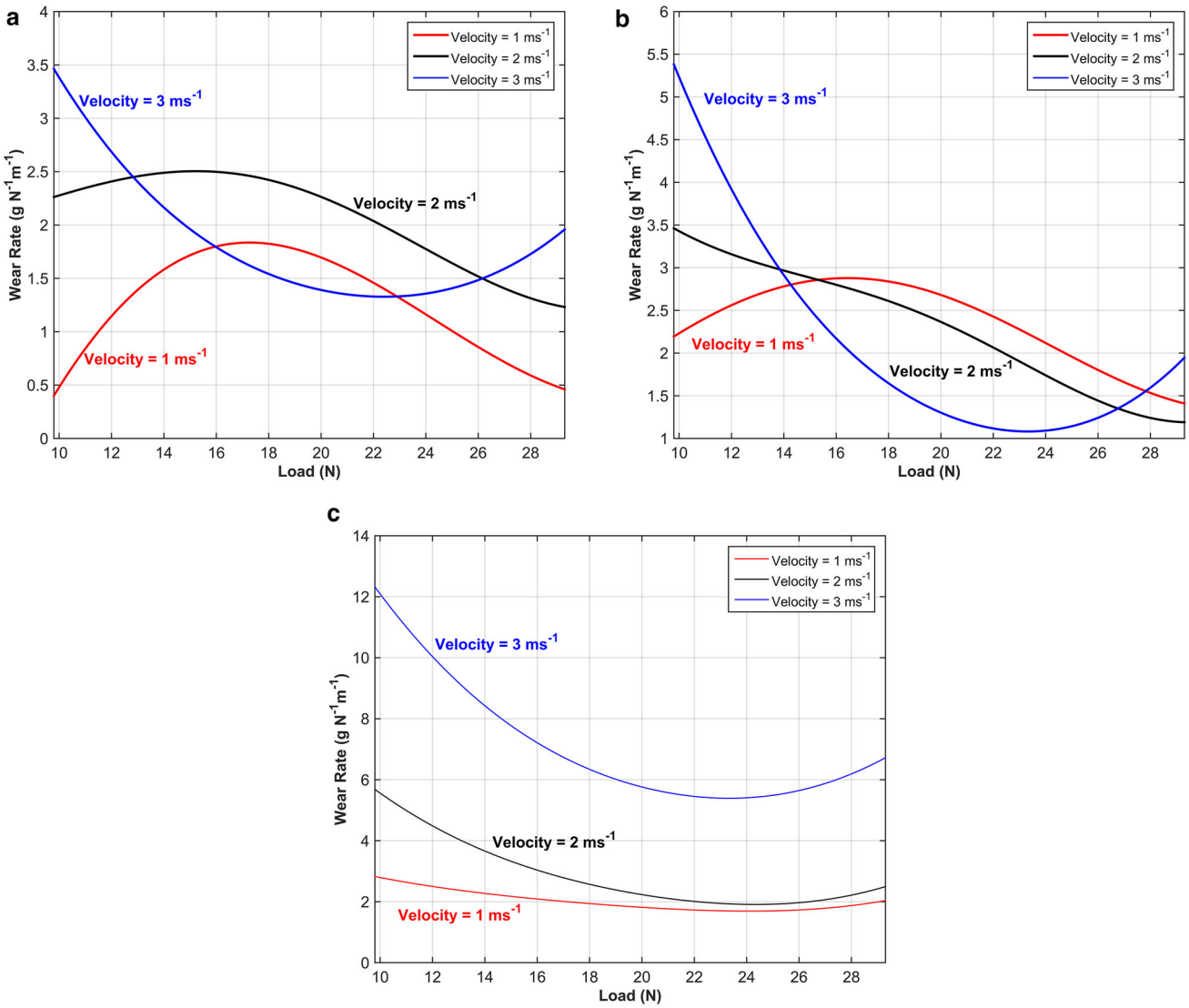

Figure 7. Effect of axial load and sliding velocity on the adhesive-wear rate of specimens showing transition load at a sliding distance of: (**a**) 600 m; (**b**) 900 m and (**c**) 1200 m.

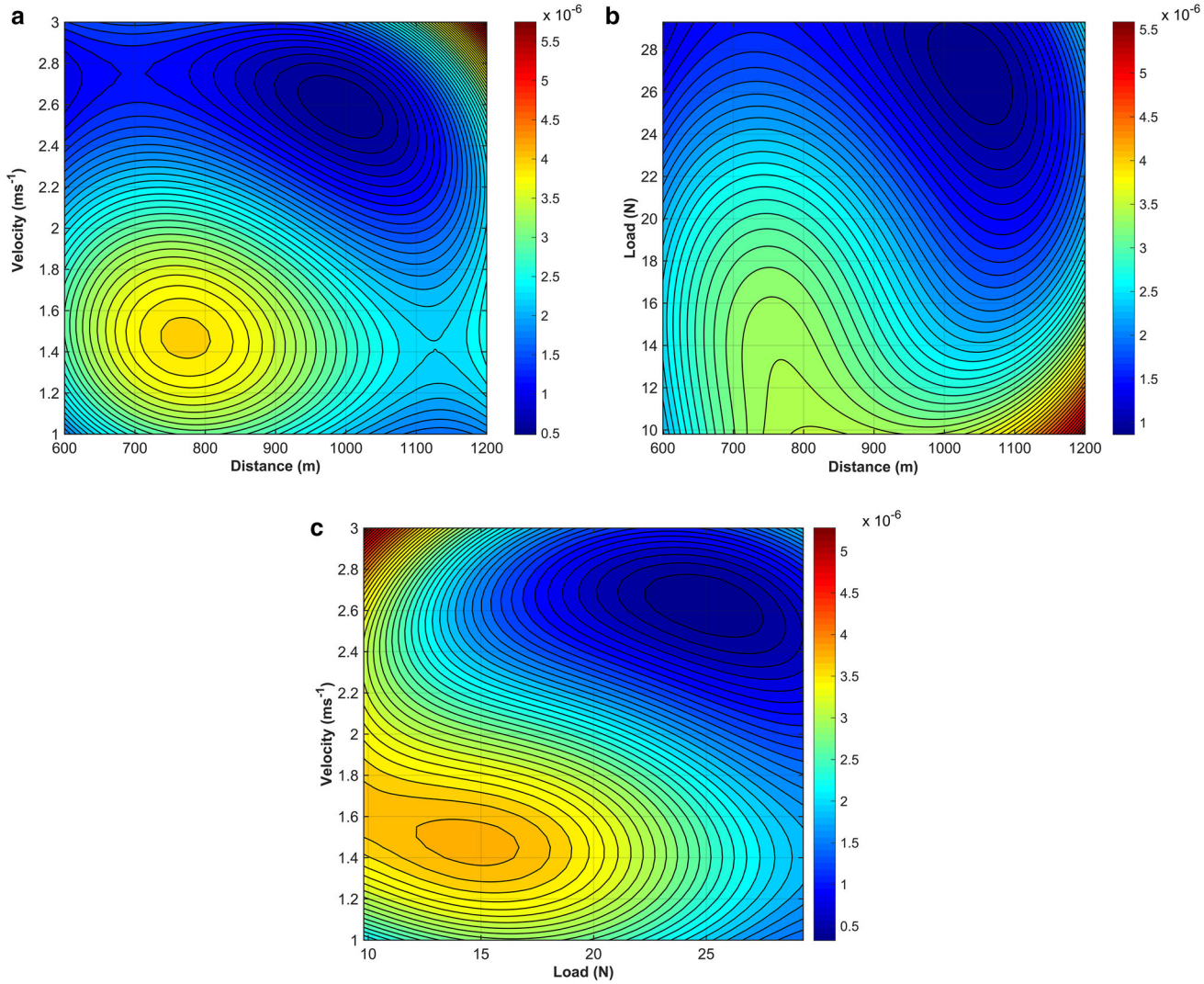

Figure 8. Effect of wear test parameters: (**a**) distance and velocity; (**b**) distance and load and (**c**) load and velocity on the wear rate of AZ91D.

debris is shown in supplementary figure S6. The XRD peaks confirmed the presence of the α phase, β phase and MgO, which indicated that the delamination of the surface oxide layer and subsurface material layer during the wear process. The broadening of the peaks indicated the plastic deformation of the material during the adhesive wear test.

A hybrid model composed of polynomial function and RBF was developed using the experimental data to investigate the influence of wear-test parameters on the wear mechanism and wear rate of the specimens. The model is given by equation (10) and was developed with the coded level of the wear-test parameters.

$$\begin{aligned}\text{Wear} = {} & 1 + 2 \times \text{Distance} + 6 \times \text{Load} + 9 \times \text{Velocity} \\ & + 4 \times \text{Distance} \times \text{Load} + 5 \times \text{Distance} \times \text{Velocity} \\ & + 8 \times \text{Load} \times \text{Velocity} + \text{RBF} \qquad (10)\end{aligned}$$

The RBF network was developed using a multiquadratic kernel with 0 centre, a global width of 2 and regularization parameter of 0.0001. The root mean squared error (RMSE) and coefficient of determination (R^2) are the critical statistical factors that determine the prediction efficiency of the developed model. The R^2 value of the model was calculated to be 0.97 and the RMSE value of the predicted value was found to be 0.03. Closeness of the R^2 value to one and closeness of the RMSE value to zero indicated the high-prediction efficiency of the developed model.

The load at which the wear of the specimen changes either from mild wear to severe wear or from severe wear to mild wear is known as the transition load. The effect of load on the wear rate of the specimens at various sliding velocities for a sliding distance of 600 m is shown in figure 7(a). The specimens tested exhibited a transition load of 19.6 N at all sliding velocities. The wear phenomenon changed from severe wear to mild wear at sliding velocities of 1 and 2 m s^{-1}

Table 5. Experimental results of the corrosion–wear test.

Sl. no.	Coded			Real			Corrosion wear rate (10^{-6}), g N^{-1} m^{-1}
	Load, N	Velocity, m s^{-1}	Distance, m	Load, N	Velocity, m s^{-1}	Distance, m	
CW1	−1	−1	−1	9.8	1	600	2.17
CW2	−1	1	1	9.8	3	1200	2.41

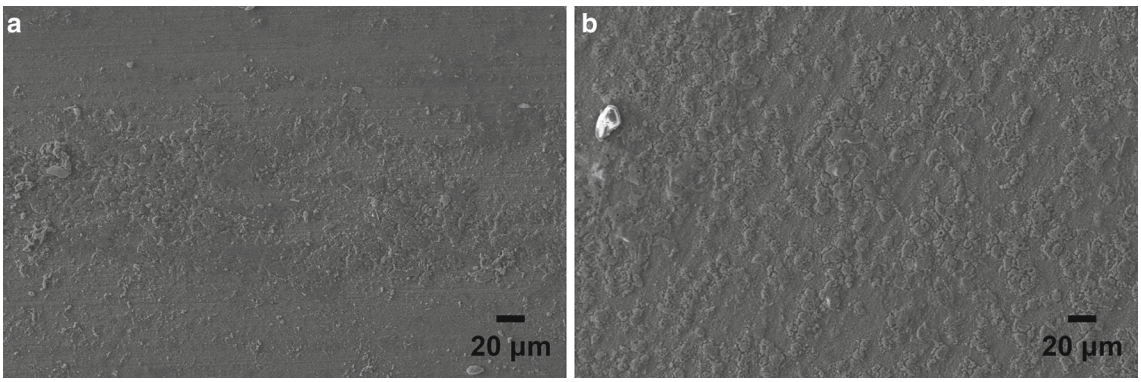

Figure 9. FE-SEM image of the specimen: (**a**) CW1 and (**b**) CW2 after the corrosion–wear test.

and changed from mild wear to severe wear at a sliding velocity of 3 m s^{-1}. The effect of load on the wear rate of the specimens at various sliding velocities for a sliding distance of 900 m is shown in figure 7(b). The specimens tested exhibited transition loads of 19.6 and 23 N at sliding velocities of 1 and 3 m s^{-1}, respectively. The wear phenomenon changed from severe to mild wear at 1 m s^{-1} and changed from mild to severe wear at a sliding velocity of 3 m s^{-1}. The wear rate decreased with an increase in load at a sliding velocity of 2 m s^{-1}. The effect of load on the wear rate of the specimens at various sliding velocities for a sliding distance of 1200 m is shown in figure 7(c). The transition load for the change in the wear phenomenon from severe to mild wear for the specimens tested was 19.6 N at sliding velocities of 2 and 3 m s^{-1}. However, no specific change in the wear phenomenon was observed for the specimens tested at a sliding velocity of 1 m s^{-1}.

The effect of the sliding distance and sliding velocity on the wear rate of the specimens is shown in figure 8(a). At a low load of 9.8 N, the wear rate increased with an increase in the sliding distance. In a mild-wear regime, the wear mechanism transforms from oxidational wear to delamination wear. However, at loads greater than 19.6 N, the wear rate decreased with an increase in the sliding distance. An increase in the wear resistance of the specimen slid for more distance at higher loads indicated the formation of a work hardened matrix layer. The effect of the sliding distance and sliding velocity on the wear rate of the specimens is shown in figure 8(b). It is observed that the wear rate decreased with an increase in the sliding velocity. The work hardening of specimens with a more slid distance decreased their wear rate. The softness of the material matrix resulted in a high-wear rate for the specimens that slid less than 900 m, at slow-sliding velocities of 1 and 2 m s^{-1}. Figure 8(c) shows the effect of the applied load and sliding velocity on the wear rate of the specimens. It is observed that the wear rate was high for the specimen tested at low load and high-sliding velocity and low for the specimen tested at high load and high-sliding velocity.

3.4 *Corrosion–wear*

The corrosion–wear tests were conducted in the SBF environment, adopting the wear-test parameter combinations that resulted in the most and the least adhesive-wear rate. The chosen level of wear-test parameters and the corresponding corrosion–wear rate are given in table 5. It is observed that the corrosion–wear of the specimens was influenced by the SBF solution. The surface morphology of the specimens CW1 and CW2 are shown in figure 9(a) and (b), respectively. It is observed that the surface of the specimens CW1 and CW2 was devoid of wear tracks and the friction coefficient was lower for the specimens subjected to the corrosion–wear test than the specimens subjected to the adhesive wear test.

The interaction of SBF with the specimen produced debris and striations on the surface. The striations were higher in the specimen CW2 than the specimen CW1. Correspondingly, the corrosion–wear rate was higher in the specimen CW2 than the specimen CW1. However, the corrosion–wear rate of specimen CW1 was higher than the specimen AW1, which had

undergone adhesive wear. The lubricating action of the SBF solution reduced the friction coefficient between the specimen and the counter disc as well as the heat generated at the specimen–counter disc interface. This resulted in a less corrosion–wear rate of the specimen CW2.

4. Conclusions

The microstructure, microhardness and TS of the magnesium alloy AZ91D were characterized. The base material was subjected to the corrosion test, wear test and combined corrosion–wear test. The conclusions of the study are as follows:

- The microstructure of the magnesium alloy AZ91D consists of α-Mg, β-$Mg_{17}Al_{12}$ and (α + β) eutectic phases. The β phase is distributed as coarse continuous precipitates in the matrix.
- The magnesium alloy AZ91D favours the formation of a hydroxyapatite layer on its surface with an increase in the immersion time in body fluids. The corrosion potential and the corrosion rate interpolated from the Tafel region is −1.448 V and 4.44 mm $year^{-1}$, respectively.
- Statistical modelling of the adhesive wear test elucidates the transition load with respect to the change in wear-test parameters. SBF has a significant influence on the wear test of the specimens, as observed from the corrosion–wear test.

Acknowledgements

The authors are grateful to Amrita Vishwa Vidyapeetham, India for their financial support to carry out this investigation through an internally funded research project no. AMRITA/IFRP-20/2016–2017.

References

[1] Anon 2014 *Essential readings in magnesium technology* (United States: Wiley)
[2] Niinomi M 2010 *Metals for biomedical devices* (United Kingdom: Elsevier)
[3] Westengen H and Rashed H M M A 2016 in *Materials science and materials engineering* (Netherlands: Elsevier) p 1
[4] Witte F and Eliezer A 2012 in *Degradation of implant materials* Noam Eliaz (ed) (New York: Springer) p 93
[5] Glasdam S-M, Glasdam S and Peters G H 2016 in *Advances in clinical chemistry* Gregory S Makowski (ed) (Netherlands: Elsevier) p 169
[6] Ambrose C G and Clanton T O 2004 *Ann. Biomed. Eng.* **32** 171
[7] Manivasagam G, Dhinasekaran D and Rajamanickam A 2010 *Recent Patents Corros. Sci.* **2** 40
[8] Agarwal S, Curtin J, Duffy B and Jaiswal S 2016 *Mater. Sci. Eng. C* **68** 948
[9] Gu X-N, Li S-S, Li X-M and Fan Y-B 2014 *Front. Mater. Sci. China* **8** 200
[10] Hornberger H 2012 *Acta Biomater.* **8** 2442
[11] Luthringer B J C, Feyerabend F and Römer R W 2014 *Magnesium Res.* **27** 142
[12] Prakasam M, Locs J, Salma-Ancane K, Loca D, Largeteau A and Berzina-Cimdina L 2017 *J. Funct. Biomater.* **8** 44
[13] Staiger M P 2006 *Biomaterials* **27** 1728
[14] Vaira Vignesh R and Padmanaban R 2018 *Advances in mathematical methods and high performance computing* (Switzerland: Springer) p 471
[15] Vaira Vignesh R, Padmanaban R, Govindaraju M and Suganya Priyadharshini G 2019 *Mater. Res. Express* **6** 1
[16] Nishio T, Kobayashi K, Matsumoto A and Ozaki K 2002 *Mater. Trans.* **43** 2110
[17] Mabuchi M, Kobata M, Chino Y and Iwasaki H 2003 *Mater. Trans.* **44** 436
[18] Shanthi M, Lim C Y H and Lu L 2007 *Tribol. Int.* **40** 335
[19] Zafari A, Ghasemi H M and Mahmudi R 2012 *Wear* **292–293** 33
[20] Zafari A, Ghasemi H and Mahmudi R 2014 *Mater. Des.* **54** 544
[21] Chen H and Alpas A T 2000 *Wear* **246** 106
[22] Witte F, Kaese V, Haferkamp H, Switzer E, Meyer-Lindenberg A, Wirth C J *et al* 2005 *Biomaterials* **26** 3557
[23] Choudhary L, Szmerling J, Goldwasser R and Raman R K S 2011 *Procedia Eng.* **10** 518
[24] Xue D, Yun Y, Tan Z, Dong Z and Schulz M J 2012 *J. Mater. Sci. Technol.* **28** 261
[25] Walter R, Kannan M B, He Y and Sandham A 2013 *Appl. Surf. Sci.* **279** 343
[26] Tahmasebifar A, Kayhan S M, Evis Z, Tezcaner A, Çinici H and Koç M 2016 *J. Alloys Compd.* **687** 906
[27] Wen Z, Duan S, Dai C, Yang F and Zhang F 2014 *Int. J. Electrochem. Sci.* **9** 7846
[28] Padmanaban R, Vignesh R V, Arivarasu M and Sundar A A 2016 *ARPN J. Eng. Appl. Sci.* **11** 6030
[29] Vaira Vignesh R and Ramasamy P 2017 *Trans. Indian Inst. Met.* **70** 2575
[30] Buhmann M D 2003 *Radial basis functions: theory and implementations* (Cambridge, England: Cambridge University Press)
[31] Chai F, Zhang D, Li Y and Zhang W 2013 *Mater. Sci. Eng. A* **568** 40
[32] Choudhary L and Singh Raman R K 2013 *Eng. Fract. Mech.* **103** 94
[33] Cavaliere P and De Marco P P 2007 *J. Mater. Process. Technol.* **184** 77
[34] Vaira Vignesh R, Padmanaban R and Govindaraju M 2019 *Surf. Topogr.: Metrol. Prop.* **7** 1
[35] Khanra A K, Jung H C, Yu S H, Hong K S and Shin K S 2010 *Bull. Mater. Sci.* **33** 43
[36] Vaira Vignesh R, Padmanaban R and Govindaraju M 2019 *Silicon* (Published Online). https://doi.org/10.1007/s12633-019-00194-6